Roles of Surface Chemistry and Texture of Nanoporous Activated Carbons in CO 2 Capture

R. Canevesi, S. Schaefer, M. Izquierdo, A. Celzard, V. Fierro

Roles of Surface Chemistry and Texture of Nanoporous Activated Carbons in CO_2 Capture

R. L. S. Canevesi[1,*], S. Schaefer[1], M.T. Izquierdo[2], A. Celzard[1], V. Fierro[1,*]

[1]Université de Lorraine, CNRS, IJL, F-88000 Epinal, France

[2]Instituto de Carboquímica, Zaragoza E-50018, Spain

[*] Corresponding author. Tel: + 33 329 29 61 77.Fax: + 33 329 29 61 38.

E-mail address: rafael-luan.sehn-canevesi@univ-lorraine.fr (R.L.S. Canevesi); vanessa.fierro@univ-lorraine.fr (V. Fierro)

Abstract

The presence of heteroatoms, such as nitrogen or oxygen, on the surface of nanoporous activated carbons (ACs) promotes CO_2 uptake due to the stronger specific interactions between these heteroatoms and the adsorptive. However, heteroatom doping post-treatments often decrease the surface area and pore volume of ACs, and it is difficult to separate heteroatom doping from textural effects. The objective of this paper was to investigate when the control of adsorption shifts from surface chemistry to textural characteristics. For this purpose, three different types of commercial ACs were doped with nitrogen and/or oxygen by an easy and cheap method and then subjected to CO_2 adsorption experiments up to 32 bar at 273K. We evaluated the effect of the surface chemistry and texture, considering the whole range of porosity, on CO_2 adsorption as a function of pressure. Below atmospheric pressure, CO_2 adsorption is mainly controlled by surface chemistry, increasing with O+N content, and the narrowest pores are responsible for more than 60% of CO_2 adsorption at pressures below 0.01 bar. Above atmospheric pressure, from 1 to about 5 bar, the textural properties become more and more significant to finally take control of the adsorption phenomena at pressures above 5 bar. We have undoubtedly shown that the adsorption capacity is only a function of the total pore volume and that the adsorbed density is even higher than that of liquid CO_2 in ultramicropores (pore diameter less than 0.7 nm) at pressures of 15 bar and above.

Keywords: CO_2 capture; activated carbons; textural properties; heteroatom content

1. Introduction

One of the most important challenges currently facing the scientific community is how to mitigate the high levels of CO_2 emissions into the atmosphere. CO_2, considered one of the most important greenhouse gases[1], comes mainly from the burning of fossil fuels such as coal, oil and natural gas, and is co-responsible for the current global warming of our planet[2]. Thus, over the past few centuries, the atmospheric CO_2 concentration has steadily increased from less than 300 ppm in the pre-industrial era, in the mid-1800s, to over 400 ppm in 2016[3]. Most scientists agree that CO_2 emissions need to be reduced by 30–60% by 2050 to keep the CO_2 concentration in the atmosphere below 550 ppm[4]. Carbon Capture and Storage (CCS) alone has the potential to reduce by about 20% the CO_2 emissions by 2050[3]. The number of commercial CCS facilities has increased from 22 in 2014 to 65 in 2020, representing a total CCS capacity of 40 Mt CO_2/year[1,5]. This capacity should be increased up to 5635 Mt by 2050 in the IEA sustainable development scenario[5]. The three main strategies to achieve CO_2 capture are absorption by solvents[6], separation by membranes[7] and adsorption on high-surface area materials[8,9]. Nowadays, the most developed is CO_2 absorption by amine-based liquids[6,7] due to their high selectivity and CO_2 absorption capacity, chemical resistance, ease of regeneration and low cost[10,11].

A competing CO_2 capture technology should reduce energy consumption for regeneration, have higher capture capacity, be easier to handle, and have a reduced environmental impact, among others[12]. Adsorption could be a realistic alternative depending on the adsorbent considered[13,14]. A large number of adsorbent types, such as zeolites[15,16], activated carbons (ACs)[17,18], metal-organic frameworks (MOFs)[16,19], porous polymers[20] and mesoporous oxides[16,21] are applied in CCS processes. ACs are a very promising class of adsorbents for CO_2 capture due to their various advantages such as low cost, easy regeneration, moisture

resistance and high mechanical strength. The successful application of an AC for CO_2 capture depends on its adsorption capacity and selectivity [22–24].

The CO_2 adsorption capacity is well correlated with the textural properties of the adsorbent, more precisely with the amount of micropores narrower than 0.7 nm[9,25–27] and the content of basic heteroatoms on the surface[28–32]. Thus, one of the most commonly used strategies to improve the adsorption capacity and selectivity of ACs for CO_2 is to increase their surface basicity by N doping[33,34]. Nitrogen can be naturally present in carbon precursors[28,35–38] or incorporated in a second step at sufficiently high temperatures that reactions occur when the carbonaceous material is in contact with a nitrogen-rich gas (*i.e.*, NH_3 or HCN)[39,40] or nitrogen-rich compounds such as urea[41,42]. Although the presence of microporosity and heteroatoms in ACs has a positive effect on CO_2 adsorption[34,41–43], it is difficult to identify the benefits of each separately[28,29,44,45]. In addition, most studies have been performed at atmospheric pressure, in which the effect of working pressure has often been neglected[46]. Depending on the pressure, an expensive doping treatment could be irrelevant or even disadvantageous, as the micropore volume and surface area could be significantly reduced after doping.

With this in mind, the present study has two main objectives: (a) to elucidate the effect of doping on textural properties; and (b) to elucidate the effect of both heteroatom content and texture on CO_2 adsorption capacity. Three commercial ACs were selected and doped with nitrogen using urea, assisted or not by a preliminary oxidation step in order to increase the reactivity of carbon. Their textural properties and elemental compositions were investigated, and their CO_2 adsorption isotherms were obtained up to 32 bar at 273K. The final panel of 14 ACs with different textures and heteroatom contents allowed us to extract clear conclusions about the effect of each factor on CO_2 adsorption as a function of pressure.

2. Materials and methods

2.1 Pristine activated carbons

Three commercial activated carbons (ACs), named MSP-20X, MSC-30 and CW30, were used as oxygen-and nitrogen-doped AC precursors. The former two ACs were supplied by Kansai Coke & Chemicals^{TM} (Japan), and the latter was provided by Silcarbon & Aktivkohle (Germany).

2.2 Chemical modifications

ACs doped with oxygen and/or nitrogen were prepared by chemical and/or thermal treatment, according to the three following routes that are schematized in Figure 1:

- O-doped carbons were prepared by oxidizing 3g of AC with a hydrogen peroxide solution (31 wt.%, VWR) at room temperature without stirring. For this, 10 mL of H_2O_2 solution was added at 1h intervals until 30 mL were poured onto the AC. 1h after the last addition, the AC was washed with distilled water and dried overnight in a ventilated oven at 378K. The resulting materials were labeled using the name of the pristine AC followed by O (*e.g.*, oxidized MSP-20X was labeled MSP-20X-O).
- N-doped carbons were obtained using urea as the N doping agent. Urea crystals (99.5 % purity, ACROS) were first ground with a PM 100 planetary ball mill (RETSCH) and sieved to a particle size less than 100 µm. 1g of AC was then mixed with urea powder, using a urea to AC weight ratio of 1 or 2. Once the blend was obtained, it was subjected to heat treatment in a tube furnace heated to 623K at a heating rate of 5K min^{-1}, and flushed with synthetic air at 50 cm^3 min^{-1}. The final temperature was maintained for 3h, after which the samples were cooled to room temperature under the same air flow. Finally, the materials were washed with hot water to neutral pH and dried overnight in a ventilated oven at 378K, as described elsewhere[47]. The resulting materials were labeled using the

name of the pristine material followed by U and the ratio of urea applied, 1 or 2, (*e.g.*, N-doped MSP-20X was labeled MSP-20X-U1 or MSP-20X-U2).

- O-N-doped carbons were obtained by mixing 1g of the O-doped carbons with urea powder, and subjecting the blend to the same protocol as described above. The resulting materials were labeled using the name of the pristine material followed by O and U2, as we only used an AC/urea weight ratio of 2 (*e.g.*, O-N-doped MSP-20X was labeled MSP-20X-OU2).

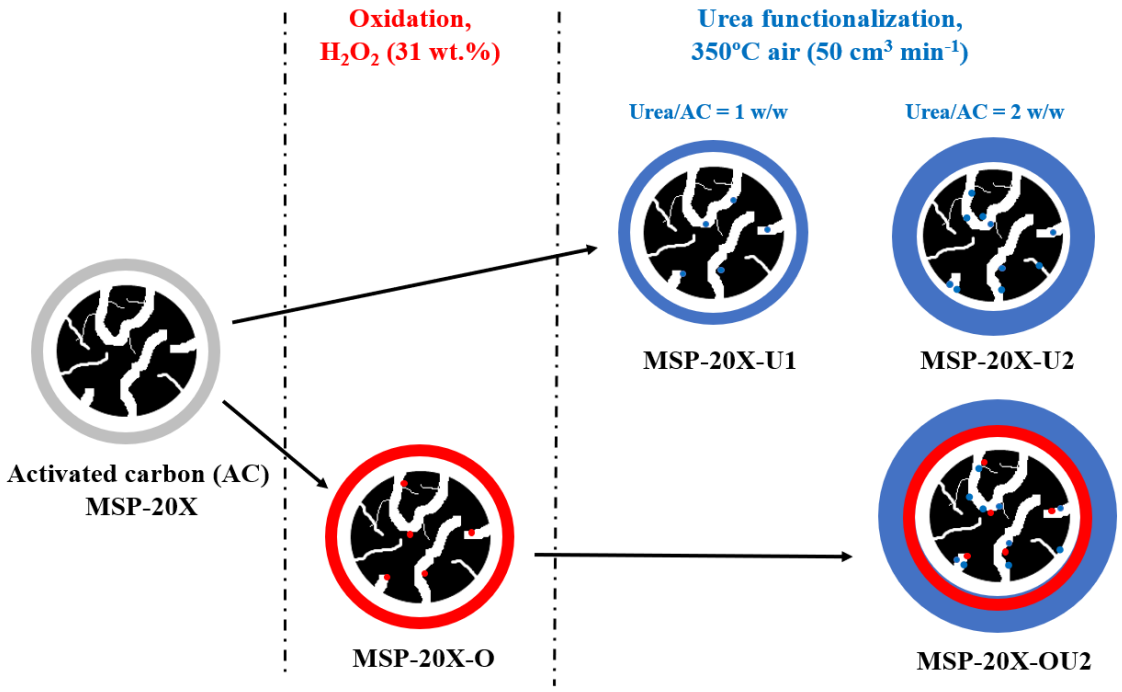

Figure 1. Scheme of the chemical/and or thermal treatments applied and the nomenclature used, MSP-20X being taken here as an example.

2.3 Adsorbent characterization

Nitrogen and hydrogen adsorption isotherms at 77K were obtained after outgassing under secondary vacuum at 383K for at least 48h by using an ASAP 2020 automatic adsorption device from Micromeritics. The specific surface area was determined either from N_2 isotherms by applying the BET equation to obtain A_{BET} (m^2 g^{-1}), or from both N_2 and H_2

isotherms by applying the two-dimensional Non-Local Density Functional Theory (2D-NLDFT) to obtain $S_{2D\text{-}NLDFT}$ (m^2 g^{-1}) using the SAIEUS software supplied by Micromeritics, which also allows to determine the pore size distribution (PSD). By integration of the PSD in the adequate pore diameter range, the volumes of ultramicropores (< 0.7 nm), $V_{ult\text{-}\mu icro}$ (cm^3 g^{-1}); supermicropores (0.7-2nm), $V_{sup\text{-}\mu icro}$ (cm^3 g^{-1}); micropores (< 2nm), $V_{\mu icro}$ (cm^3 g^{-1}); mesopores (2-50nm), V_{MES} (cm^3 g^{-1}) and the total volume of pores, V_T (cm^3 g^{-1}), were determined. The ultramicropore fraction, $X_{ult\text{-}\mu icro}$ (dimensionless), was calculated by the ratio of ultramicropore to micropore volumes. The micropore fraction, $X_{\mu icro}$ (dimensionless), was calculated by dividing the micropore volume by the total pore volume. The average pore diameters across the entire pore range, L_0 (nm); in the mesopore range, $L_{0\ meso}$ (nm); in the micropore range, $L_{0\ \mu icro}$ (nm); in the supermicropore range, $L_{0\ sup\text{-}\mu icro}$ (nm); and in the ultramicropore range, $L_{0\ ult\text{-}\mu icro}$ (nm); were calculated by integration of the PSDs. For comparison purposes, the micropore volume was also calculated using the Dubinin-Raduskevich (DR) equation applied to the N_2 adsorption isotherm, V_{DRN2} (cm^3 g^{-1}). More details are given elsewhere[48,49].

The carbon, oxygen and nitrogen contents on the surface were determined by X-ray photoelectron spectroscopy (XPS), using an ESCAPlus OMICROM system with a hemispherical electron energy analyzer with an analysis area of 1.75 × 2.75 mm. The spectrometer was operated at 10 kV and 15 mA, using a non-monochromatized Mg X-ray source (1253.6 eV) under vacuum (< 5×10^{-9} Torr). The CASA data processing software was used to perform smoothing, Shirley-type background subtraction, peak fitting, and quantification[50,51].

Elemental analysis (EA) was carried out with a Vario El Cube elemental analyzer (Elementar) to determine carbon, hydrogen, nitrogen and sulfur contents by combustion of the

samples in a mixture of dioxygen and helium. The oxygen content was directly quantified with the same equipment in a second step. More details are given elsewhere[52].

2.4 CO_2 adsorption isotherms

Low-pressure CO_2 adsorption data at 273K were obtained using an ASAP 2420 manometric device. Prior to measurement, the samples were outgassed under secondary vacuum (7×10^{-6} mbar) and 383K for at least 48h. High-pressure CO_2 adsorption experiments were carried out at 237K and up to 32 bar using an HPVA II manometric high-pressure device (Micromeritics). Prior to any measurement, the samples were also outgassed in the same conditions as above. After evacuation, the pressure was increased stepwise, from 0.5 to 32 bar, and then decreased in steps from 32 to 5 bar. At each step, the amount of gas adsorbed by the sample was calculated as the difference between the amounts of gas dosed and determined at equilibrium pressure. The contribution of the empty cell was systematically measured and subtracted from all data in order to improve accuracy.

2.4.1 Fitting of CO_2 adsorption isotherms

The Sips model[53] was applied to describe the experimental data obtained to better understand the relevant factors affecting the CO_2 adsorption capacity. The Sips isotherm is a combination of the Langmuir and Freundlich isotherms and it introduces a finite adsorption limit to the Freundlich equation; the mathematical form of the model is:

$$q = \frac{q_s k_s p^{1/n_s}}{\left[1 + k_s p^{1/n_s}\right]} \qquad (1)$$

where q_s (mol g^{-1}) is a constant reflecting the saturation adsorption capacity, k_s (bar^{ns}) is the Sips constant or affinity constant, and $1/n_s$ (dimensionless) is the heterogeneity factor.

The parameters of the isotherm were obtained by nonlinear fits of the aforementioned equation to the experimental CO_2 equilibrium data with Origin version 9.0 software, using the Levenberg-Marquardt algorithm. The adsorption models leading to the best fits were identified from the obtained determination coefficient R^2, which was as close to 1 as possible.

2.4.2 Fitting of CO_2 adsorption capacities

The contributions of textural properties and surface chemistry to CO_2 adsorption capacity were evaluated as follows. First, based on PSDs, the pore volumes V_i (cm^3/g) of the materials were divided into four classes according to their pore size L (nm): $V_{L<0.5}$, $V_{0.5<L<0.7}$, $V_{0.7<L<2}$, $V_{L>2}$, and a coefficient representing the contribution to adsorption was associated with each range. Then, the contribution of surface chemistry was assigned to the addition of oxygen and nitrogen contents (C_{N+O}), obtained by XPS. Therefore, the CO_2 adsorption capacity, q (mol kg^{-1}), was represented mathematically as follows:

$$q = a_1 V_{L<0..5} + a_2 V_{0.5<L<0.7} + a_3 V_{0.7<L<2} + a_4 V_{L>2} + b C_{N+O} \quad (2)$$

At a given pressure, a multiple linear regression, based on the previous equation, was carried out on the whole set of experimentally obtained data (V_i, C_{N+O} and q), which allowed the determination of coefficients a_i and b. The coefficients a_1 to a_4 represent the average density of the adsorbed phase in each pore class, while the parameter b is directly correlated to the interaction with the nitrogen content at the surface. The model was fitted to the experimental data obtained at 10 different pressures: 0.01, 0.1, 0.5, 1, 2, 5, 7, 10, 15 and 25 bar at 273K.

3. Results and discussion

3.1 Chemical composition and its effect on texture

Figs. 2a, 2b, 2c and 2d show the nitrogen and hydrogen adsorption-desorption isotherms, PSDs and corresponding cumulative pore volumes, respectively, of the non-doped ACs. MSP-20X and MSC-30 had type Ia and Ib nitrogen isotherms, *i.e.*, characteristic of microporous materials according to the IUPAC classification[54], without a hysteresis loop. The main difference between them was the relative pressure at which the adsorption plateau is reached: 0.1 for MSP-20X and 0.4 for MSC-30. MSC-30 is then a super-activated carbon with a highly developed pore texture and a high fraction of supermicropores and narrow mesopores. CW30 showed a type IV isotherm and exhibited a hysteresis loop at relative pressures above 0.50, suggesting the presence of capillary condensation in the mesopores.

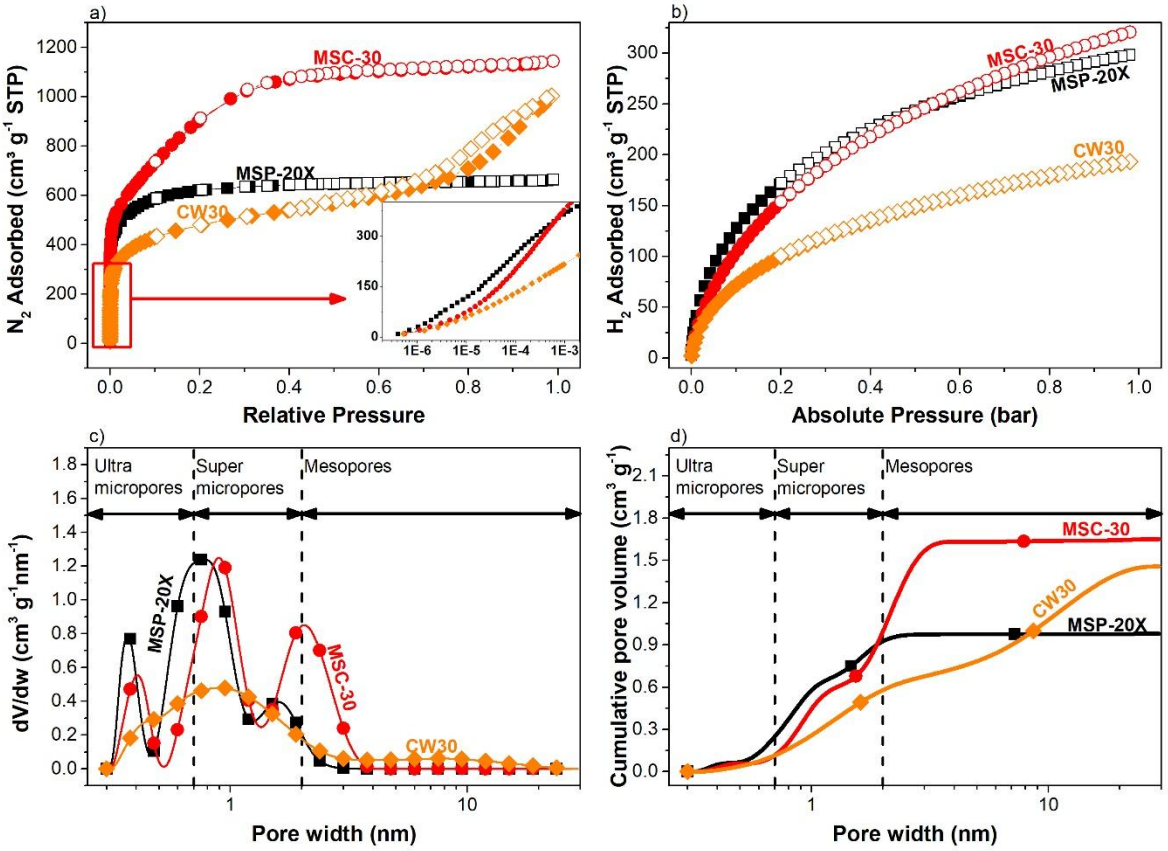

Figure 2. Adsorption (full symbols) and desorption (empty symbols) isotherms at 77K of: (a) nitrogen, and (b) hydrogen; (c) pore size distributions, and (d) cumulative pore volumes calculated by the 2D-NLDFT model, of pristine commercial activated carbons. The insert in (a) shows nitrogen isotherms up to a relative pressure of 10^{-3}.

The textural properties of doped and non-doped materials (specific surface area, total pore volume, micropore volume, etc.) are gathered in Table SI 1 of the Supplementary Information. High values of surface area $S_{2D\text{-}NLDFT}$, between 1032 and 2522 $m^2\ g^{-1}$, and of total pore volume $V_{T\ 2D\text{-}NLDFT}$, from 0.67 to 1.60 $cm^3\ g^{-1}$, were found. The MSP-20X-derived materials were mostly microporous (x_{micro} ranging from 93 to 95%.), the MSC-30-derived materials showed significant content of micropores (x_{micr} ranging from 61 to 68 %.), and those derived from CW30 showed a much lower content of micropores (x_{micro} ranging from 39 to 49 %). Urea treatment decreased the values of $S_{2D\text{-}NLDFT}$ of the pristine ACs, and thus the urea / AC weight ratios of 1 and 2 decreased them by 15-24 % and 20-28 %, respectively.

Fig. 3 shows the nitrogen and hydrogen isotherms at 77K as well as the PSDs and cumulative pore volumes of the MSC-30 series: pristine MSC-30 AC and ACs doped with N, O and N + O. Urea treatment induced a progressive decrease in average micropore size that can be seen by the changes at the knee angle of the nitrogen isotherm at low relative pressures ($p/p_0 < 0.2$) (Fig. 3a) and confirmed by the PSDs (Fig. 3c). This suggests a gradual micropore hindrance. N and O doping also decreased the pore volume of the other two series of materials, as can be seen in Figs. SI 2 and SI 3 in the Supporting Information. MSC-30-O showed this effect less intensely than the N-doped ACs, showing that hindrance is mainly due to the N-functional groups. Thus, the PSD of MSC-30-U2 is almost identical to that of MSC-30-OU2.

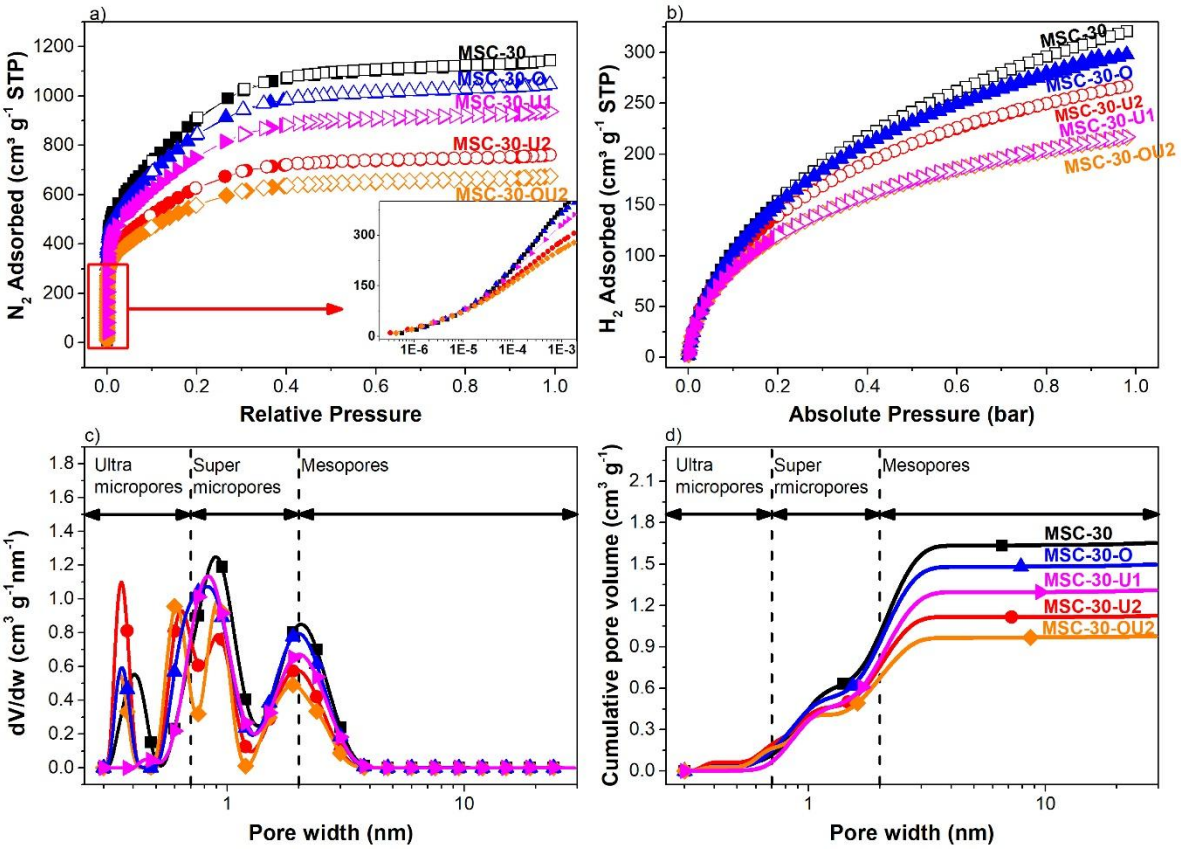

Figure 3. Same as Fig. 2, but for the pristine MSC-30 and derived MSC-30-doped ACs.

The bulk composition (C, H, O, N and N+O) of the pristine and doped ACs, measured by elemental analysis, is presented in Table SI 4. The O content in the pristine ACs varied from 3.4. to 19.5 wt. %, for MSP-20X and CW30 respectively, whereas the N content was never higher than 0.3 wt. % and the presence of S content was never detected. A slight reduction in carbon mass was observed after the oxidation treatment, less than 5%, but urea doping did not significantly change the final mass. In agreement with previous studies[55,56], the O content increased dramatically after oxidation with H_2O_2 and was 12.9, 13.7 and 28.0 wt. % for MSP-20X, MSC-30 and CW30, respectively. In the absence of preliminary oxidation, increasing the urea / carbon weight ratio had a positive impact on the N content, as seen for the series MSP-20X and MSC-30. Indeed, ACs doped with a urea / carbon weight ratio of 1 showed an N content close to 7 wt. %, while those prepared with a ratio equal to 2 showed an N content ranging from 10.5 to 15.1 wt. %. N doping was significantly favored by the presence of

oxygen (see Tables SI 4 and SI 5), confirming that O plays a major role in N incorporation due to Hofmann rearrangements, as previously reported[57,58]. The N content further increased to 13.2 and 16.5 wt.% for MSP-20X-OU2 and CW30-OU2, respectively. A similar increase in O and N contents was determined by XPS (Table SI 5), indicating that N doping occurred primarily on the carbon surface.

The doping treatments modified both their chemical and textural properties. The ACs with the highest N and O contents (CW30-OU2 and CW30-U2) also presented the most reduced textural properties (*i.e.*, A_{BET}, $S_{2D\text{-}NLDFT}$, $V_{sup\text{-}\mu icro}$ and $V_{\mu icro}$). Figs. 4a and 4b show the linear reduction of $S_{2D\text{-}NLDFT}$ and A_{BET}, respectively, with the N + O content determined by elemental analysis. The determination coefficient, R^2, was higher when plotting $S_{2D\text{-}NLDFT}$, 0.85, than when plotting A_{BET}, 0.76, due to the limitations of the BET model but also due to the fact that $S_{2D\text{-}NLDFT}$ was calculated from the N_2 and H_2 isotherms at 77K, which give a more accurate picture of the texture in doped ultramicroporous materials[59,60]. The reduction in surface area after urea treatment may be due to the incorporation of O and N groups grafted at the edges of the carbon layers, which would induce a steric hindrance and thus a reduced access to the micropores [61,62]. This is in good agreement with the XPS analysis of the doped ACs, mainly showing carbonyl (532.5 ± 0.4 eV and 531.2± 0.4 eV) oxygen groups (Table SI 6) and pyridinic (398.5 ± 0.4 eV) and pyrrolic (400.5 ± 0.3 eV) nitrogen groups (Table SI 7)[50,63]. Comparing the bulk and surface compositions (Fig. 4c), it can be observed that the determination factor of the linear correlation between them follows the order MSP-20X > MSC-30 > CW30, which is in agreement with the lower correlation obtained between the surface composition and $S_{2D\text{-}NLDFT}$ (Fig. 4d). The latter behavior may be due to the formation of multilayered clusters of heteroatoms in materials of lower $S_{2D\text{-}NLDFT}$. Fig. 4e thus shows the linear reduction in micropore volume as a function of the O+N content (R^2 equal to 0.9). The mesopore volume also decreased with O+N doping, but with different slopes depending on

the mesoporous fraction of the pristine ACs (Fig. 4f). Since the change in pore volume mainly affects the mesopores and supermicropores (see again Fig. 3d), this indicates that O and N heteroatoms are more likely to be incorporated into the wider pores. This hypothesis is also supported by the fact that the ultramicropore content increased with doping (see again Table SI 1), which could be due to pore hindrance by the increase in ultramicropore volume due to the shrinkage of supermicropores.

On the other hand, the average micropore size of MSP-20X-derived ACs remained almost constant with N+O content while a significant decrease in the average micropore size for ACs derived from MSC-30 and CW30 was observed (see again Table SI 1). These different behaviors indeed support that the doping occurred mainly in the widest pores. In this way, Fig. SI 8 proposes a very simplified mechanism of pore narrowing after nitrogen and oxygen doping. The presence of surface groups such as amine, amide, carboxyl and hydroxyl groups are likely to occupy the pore volume while functional groups containing ether, pyrrole and pyridine groups are, based on simple geometrical considerations, likely to distort the carbonaceous pore structure. These types of functionalities are common in O- and N-doped ACs[64], inducing steric hindrance and local deformation of the carbon structure, which implies shrinkage and eventual blockage of the pores. Table SI 9 gathers all the determination coefficients corresponding to the correlations stablished between the textural and chemical properties of the ACs.

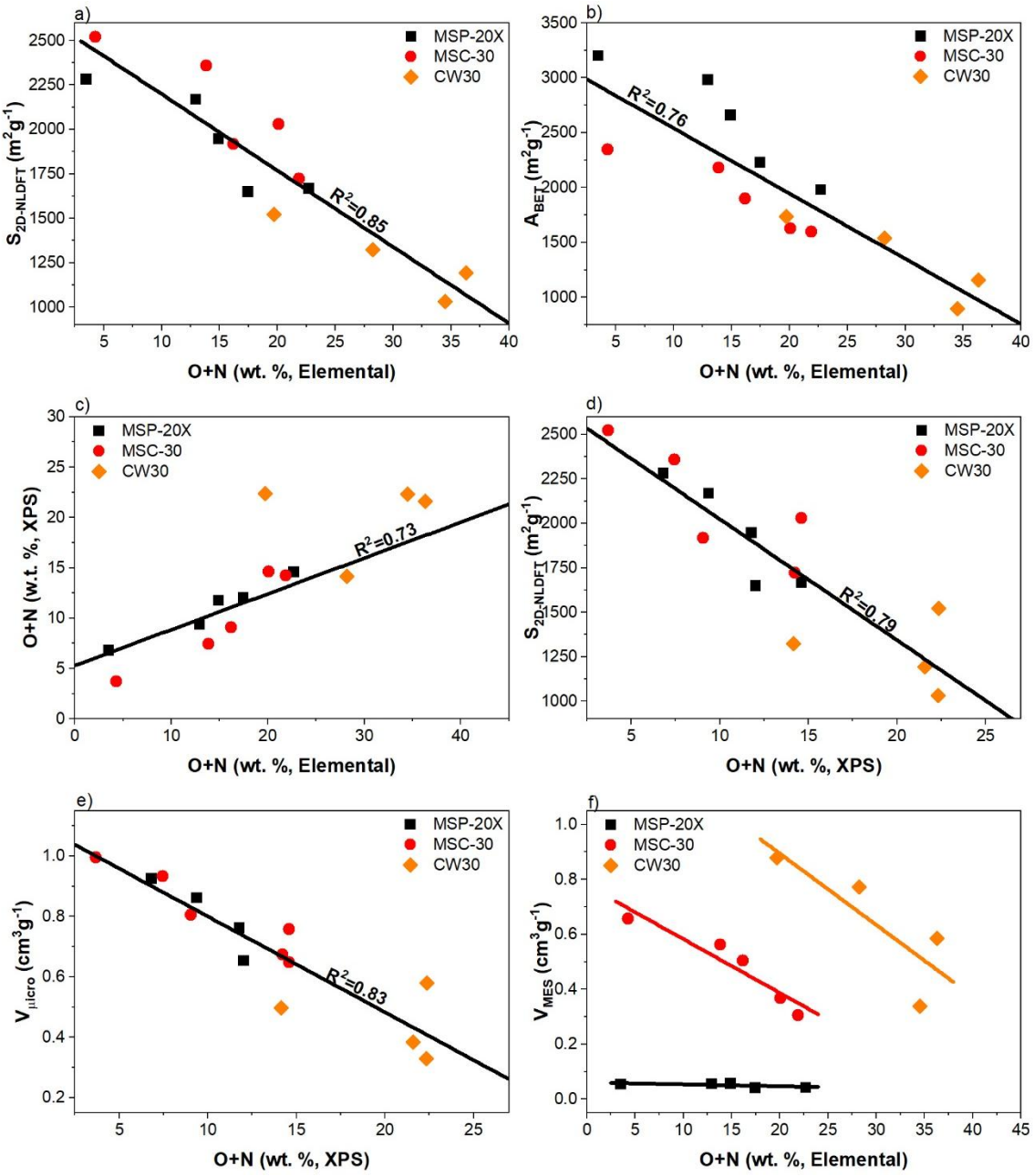

Figure 4. Effect of the O+N content (determined by EA) on: (a) 2D-NLDFT surface area; and (b) BET area. (c) Relationship between O+N contents determined by AE and XPS; (d) $S_{2D\text{-}NLDFT}$; and (e) $V_{\mu icro}$ as a function of O+N content (determined by XPS). (f) V_{MES} as a function of O+N content (determined by EA). Other correlations are suggested in Table SI 9.

3.2 CO_2 adsorption at 273K

The CO_2 adsorption isotherms of the three commercial ACs were performed at 273K and up to 32 bar and are shown in Fig. 5a. The CO_2 adsorption capacity at high pressure increases with $S_{2D\text{-}NLDFT}$ and thus follows the order CW30 < MSP-20X < MSC-30. Since the surface area depends mainly on the micropore volume, the material with the highest adsorption capacity is the MSC-30, which has the largest volume of micropores (Table SI 1). At the highest pressure evaluated, the wider mesopores are not completely filled, because if this were the case, CW30 should have a higher CO_2 capacity than MSP-X20, since the former AC has a V_T equal to 1.46 $cm^3\ g^{-1}$ versus 0.98 $cm^3\ g^{-1}$ for the latter. At pressures below 4 bar, the capacity of MSC-30 was lower than that of MSP-20X due to the larger volume of narrow pores present in the latter material, which are filled at lower pressures. Fig. 5b shows the reduction in CO_2 capacity at high pressure upon increasing the heteroatom content, in good agreement with the reduction in V_T shown in Fig. 3d. The other two series of ACs exhibited similar behaviors, as seen in Fig. SI 10.

However, using the linear isotherm plot, the differences are not really clear at pressures lower or equal to 1 bar. One way to assess the performance of the adsorbent in the low pressure range, 0.001 – 1 bar, is to compare the values of Henry's Law constant (H), which can be obtained using the linearized Virial equation, Eq. (3)[65]:

$$\ln\left(\frac{p}{q}\right) = \sum_{i=1}^{n} \alpha_i q - ln(H) \qquad (3)$$

where α_i (kg mol^{-1}) are the Virial parameters, p (bar) is the equilibrium adsorption pressure and q (mol kg^{-1}) is the amount adsorbed at equilibrium. Fig. 5c shows ln(p/q) versus q for the pristine ACs, where the y-axis intercept is the negative natural logarithm of Henry's law constant[65–67].

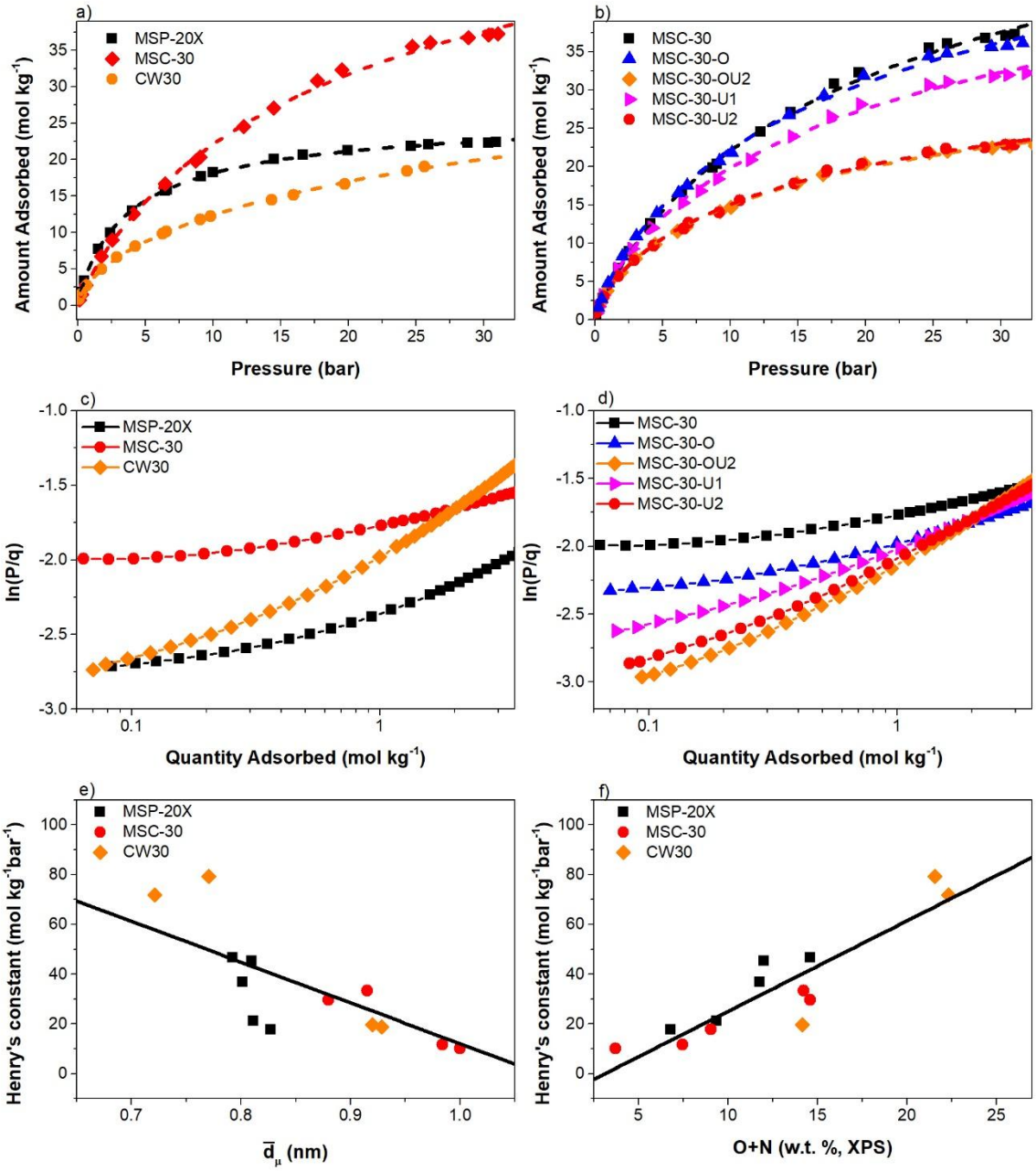

Figure 5. Experimental and fitted CO_2 adsorption isotherms at 273K and up to 30 bar of: (a) non-doped ACs; and (b) MSC-30 series. Virial plot for the adsorption isotherm in the low-pressure range of: (c) non-doped ACs; and (d) the MSC-30 AC series. Dependence of Henry's constant on: (e) average micropore diameter; and (f) O+N content at the AC surface.

Fig. 5d shows ln(p/q) versus q for the MSC-30 series, in which the materials with the highest Henry's law constant are the doped ACs. Similar behavior is also shown by the other two series of ACs (see Fig. SI 11). These trends could be due either to the increased fraction of micropores wider than 0.7 nm, as mentioned above, or to enhanced interactions with the more heteroatom-rich surfaces. Both hypotheses are illustrated in Figs. 5e and 5f where it is respectively possible to see a clear correlation between the Henry constant and the average micropore diameter on the one hand, and the heteroatom content on the other hand.

The CO_2 adsorption data of pristine and doped ACs were fitted by the Sips model to obtain n_s, k_s and q_s, and the values of the corresponding determination coefficients were in all cases very close to unity (see Table SI 12). Fig. 6a shows the linear dependence (R^2 = 0.83) of n_s (dimensionless) with the O+N content, due to an increase in surface heterogeneity.

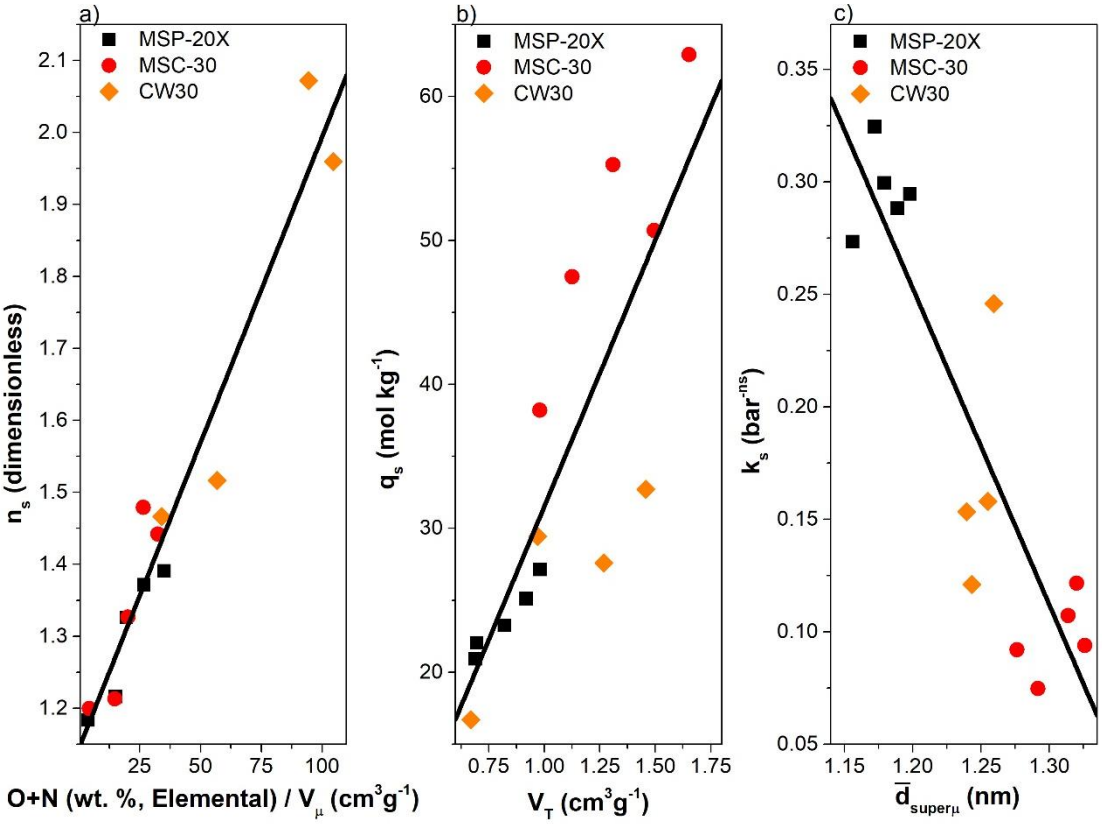

Figure 6. Sips isotherm parameters: (a) n_s: (b) q_s; and (c) k_s, as a function of the ratio of O+N content to micropore volume, total pore volume, and supermicropore diameter, respectively. Other correlations are shown in Table SI 13.

Fig. 6b shows the linear relationship of q_s (mol kg^{-1}) with V_T (R^2 = 0.68); although the determination factor is not high, it is higher than that found with $S_{2D\text{-}NLDFT}$. This is due to the fact that not only adsorption but also pore filling plays a role at pressures higher than 30 bar, even though not all pores are filled with CO_2, and this explains the relatively low determination factor. Fig. 6c shows that k_s (bar^{-ns}) decreases linearly (R^2 = 0.77) with the average supermicropore diameter due to an increase in affinity between adsorbent and adsorbate for the materials having a low average micropore diameter. Correlations between the three Sips parameters and the other textural and chemical properties are presented in Table SI 13.

3.3 Joint effect of textural and chemical properties on CO_2 adsorption

Due to the obvious effect of surface chemistry on the textural properties presented in Section 3.1, and in order to assess the effect of both on the CO_2 adsorption capacity, the uptakes obtained by the pristine and doped ACs were normalized by $S_{2D\text{-}NLDFT}$ and V_T. Figs. 7a and 7b show the dependence of the amount of CO_2 adsorbed per unit of surface area and micropore volume, respectively, for all materials at 273K and different pressures (0.1, 1.0, 5.0, 10 and 25 bar) as a function of the surface N+O content and average pore diameter, respectively. The uptakes obtained at each pressure and used for further analysis are shown in SI 14. These figures evidence that increasing the N+O content linearly affects the CO_2 adsorption capacity per surface area and per micropore volume in the low-pressure range (0.1 – 1 bar). The effect of N+O arises from the strong polar interactions between the quadrupole moment of CO_2 and the nitrogen- and possibly oxygen-containing groups[68]. The increase in this interaction is strongly related to the basic character of certain nitrogen-containing surface

groups that preferentially interact with CO_2[35]. Such an increase in permanent polar interactions can induce a local increase in the amount adsorbed. At low pressure, the decrease in textural properties due to heteroatom doping is balanced by this increase in adsorbed amount as observed in imine-based ACs[69]. However, while the N+O content has a minor effect at pressures above 5 bar, the average adsorbed density becomes linearly dependent on the average pore diameter (Fig. 7b). This supports the fact that surface chemistry plays an important and positive role at low pressure, and that this effect gradually disappears with increasing pressure, where the role of pore volume becomes increasingly important. Accordingly, Hu et al.[70] reported that up to 10 bar, the CO_2 adsorption capacity of petroleum coke activated with KOH is due to the filling of larger micropores (above 0.7 nm) and mesopores (up to 4 nm).

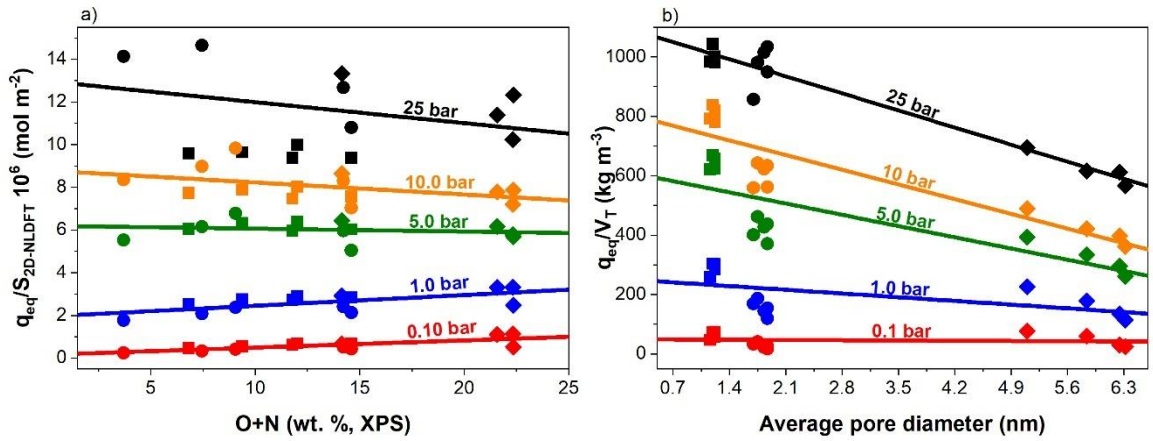

Figure 7. Amount of CO_2 adsorbed: (a) per unit of $S_{2D\text{-}NLDFT}$; and (b) per unit of V_T at 273K and 5 different pressures (0.1, 1.0, 5.0, 10 and 25 bar) as a function of the surface O+N content and average pore diameter, respectively.

At this point, it is clear that the CO_2 uptake observed on ACs is a subtle balance between physical interactions, favored by narrow pores, and chemical interactions, which are best evidenced at low pressure. To confirm the previous findings, the contributions of textural properties and surface chemistry to the CO_2 adsorption capacity were evaluated by fitting Eq.

(2) to the experimental adsorption data. The polynomial fits showed good efficiency in describing the experimental data (Fig. 8a). The coefficient related to the nitrogen and oxygen content (Fig. 8b) increased with pressure up to 1 bar, where it remained constant until the pressure of 5 bar. Above 5 bar, this coefficient suddenly decreased to near zero at 10 bar. This indicates that the effect of heteroatom doping is limited to low pressures, below 1 bar in this case. According to this multilinear regression and at pressures above 5 bar, the amount of CO_2 adsorbed depends only on the textural parameters.

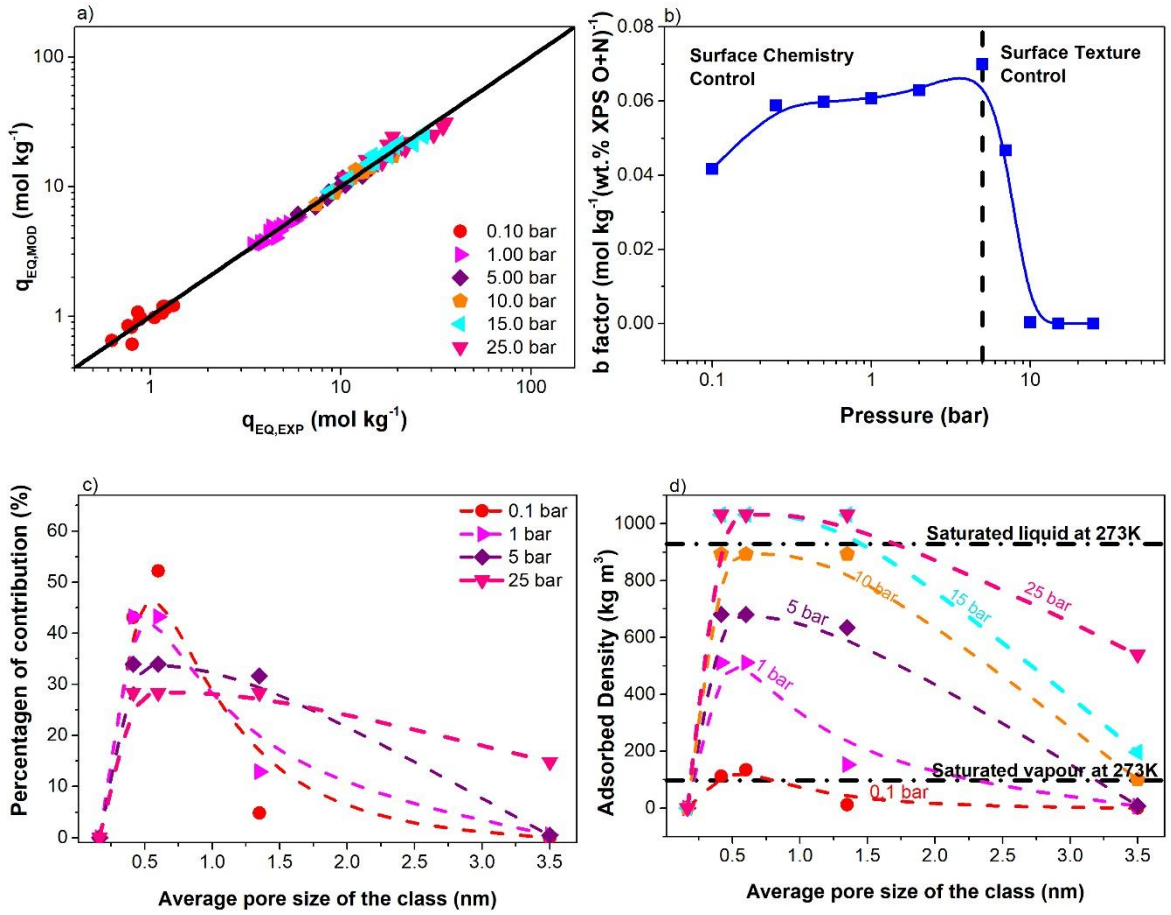

Figure8. (a) Polynomial model compared to experimental data; (b) Interaction factor (*b* factor of Eq. (2)) as a function of pressure; (c) Contributions to CO_2 adsorption from different pore sizes ranges; (d) Estimated density of the adsorbed phase at 273K and up to 25 bar.

Fig. 8c shows the contributions to CO_2 uptake (calculated from the adjustable parameters a_1 to a_4 in Eq. (2)) at 273K and pressures ranging from 0.10 to 25 bar as a function of average pore size. It can be clearly seen that ultramicropores contribute up to 60% of the uptake at low pressure while the contribution of supermicropores and narrow mesopores becomes increasingly important as the pressure increases. From the fit, it was possible to estimate the density of the adsorbed phase at different equilibrium pressures and as a function of the average pore class (Fig. 8d): a_1 for pores smaller than 0.5 nm; a_2 for pores between 0.5 and 0.7 nm; a_3 for pores between 0.7 and 2 nm; and a_4 for pores wider than 2 nm. At all the pressures, the estimated adsorbed density is higher in the narrow pore region, which is in agreement with other previous studies[9]. At 10 bar, the density thus estimated reaches values close to 980 kg m^{-3} within the ultramicropores, whereas values around 600 kg m^{-3} were reported for coals at 10 bar and 313K[71], *i.e.*, at a higher temperature than the one used in this study, and these values represent the average density of the adsorbed phase. Other authors who studied CO_2 adsorption on dry coal obtained an average density of the adsorbed phase close to 987 kg m^{-3} [72], which is very close to the values estimated here in the micropore range and at pressures above 10bar. The maximum value of the adsorbed phase density obtained here, 1031 kg m^{-3}, is higher than that of liquid CO_2 at the temperature of 273K. This maximum was reached at 15 bar and remained constant with increasing pressure.

Finally, it is important to note that the results presented here are for the temperature of 273K, and that temperature has an effect on the density of the adsorbed phase as well as on the critical pressure value that shifts the control of adsorption from surface chemistry to texture. In this sense, further experiments are being performed to study the shift of this critical pressure as a function of the working temperature, which has a major effect[8,9].

4. Conclusions

In this study, the CO_2 adsorption capacity of three commercial nanoporous ACs: MSP-20X, MSC-30 and CW30, either as received or after chemical treatment to incorporate oxygen and nitrogen, was investigated at pressures ranging from 0.01 to 32 bar at 273K. These series of ACs were selected for the diversity of their porous structures, with pristine ACs presenting BET areas ranging from 1736 to 3200 $m^2 g^{-1}$ and micropore fractions ranging from 40 to 95%. The following conclusions were drawn:

- The highest nitrogen bulk content, up to 16.5 wt. %, was obtained with materials pre-oxidized with hydrogen peroxide and then subjected to urea treatment. N- and O- doping decreased the surface area, probably due to steric hindrance and deformation affecting supermicropores and mesopores.
- Surface chemistry controls the CO_2 adsorption process at low pressure. The shift from surface chemistry-controlled to pore texture-controlled behavior at 5 bar was clearly evidenced. Future studies are needed to evaluate the effect of temperature on the value of pressure that switches the control of adsorption from one mode to the other.
- The maximum value of the adsorbed phase density obtained here, 1031 kg m^{-3}, is higher than that of liquid CO_2 at the temperature of 273K. This maximum was reached in ultramicropores (pore diameter less than 0.7 nm) at 15 bar and remained constant with increasing pressure.

Acknowledgements

This study was partly supported by ANR-15-IDEX-04-LUE and ERDF-funded project TALiSMAN (2019-000214). We acknowledge the collaboration of J.E. Monsivais Rocha in the synthesis of the materials used in this study.

Supporting information

Textural properties calculated from N_2 and H_2 adsorption isotherms for all materials in this study; N_2 and H_2 adsorption-desorption isotherms at 77K, pore size distributions and cumulative pore volumes calculated by the 2D-NLDFT model for pristine and derived MSP-20X and CW30 carbons; Bulk composition measured by elemental analysis (EA); Surface composition measured by X-ray Photoelectron Spectroscopy (XPS); Relative contribution of the different surface N- and O- groups of the materials in this study, measured by XPS; Pore narrowing and blocking mechanism due to the incorporation of N- and O- functional groups; Determination coefficients (R^2) between textural and chemical properties; CO_2 adsorption isotherms at 273K and up to 10 bar; Relative Virial plot for low-pressure CO_2 adsorption isotherms at 273K; Parameters obtained by applying the Sips model to the CO_2 adsorption isotherms; Determination coefficients (R^2) between the Sips parameters and textural and chemical properties; Experimental data set used for the analysis of the joint effect of superficial textural and chemical characteristics.

References

(1) Alami, A. H.; Abu Hawili, A.; Tawalbeh, M.; Hasan, R.; Al Mahmoud, L.; Chibib, S.; Mahmood, A.; Aokal, K.; Rattanapanya, P. Materials and Logistics for Carbon Dioxide Capture, Storage and Utilization. Sci. Total Environ. 2020, 717, 137221. https://doi.org/10.1016/j.scitotenv.2020.137221.

(2) Florides, G. A.; Christodoulides, P. Global Warming and Carbon Dioxide through Sciences. Environ. Int. 2009, 35 (2), 390–401. https://doi.org/10.1016/j.envint.2008.07.007.

(3) Aminu, M. D.; Nabavi, S. A.; Rochelle, C. A.; Manovic, V. A Review of Developments in Carbon Dioxide Storage. Appl. Energy 2017, 208, 1389–1419. https://doi.org/10.1016/j.apenergy.2017.09.015.

(4) Oh, T. H. Carbon Capture and Storage Potential in Coal-Fired Plant in Malaysia—A Review. Renew. Sustain. Energy Rev. 2010, 14 (9), 2697 – 2709. https://doi.org/10.1016/j.rser.2010.06.003.

(5) Global Status Report - Global CCS Institute; Global CCS Insitute, 2020.

(6) Scurto, A. M.; Aki, S. N. V. K.; Brennecke, J. F. CO_2 as a Separation Switch for Ionic Liquid/Organic Mixtures. J. Am. Chem. Soc. 2002, 124 (35), 10276–10277. https://doi.org/10.1021/ja0268682.

(7) Powell, C. E.; Qiao, G. G. Polymeric CO_2/N_2 Gas Separation Membranes for the Capture of Carbon Dioxide from Power Plant Flue Gases. J. Membr. Sci. 2006, 279 (1–2), 1–49. https://doi.org/10.1016/j.memsci.2005.12.062.

(8) Dou, B.; Wang, C.; Song, Y.; Chen, H.; Jiang, B.; Yang, M.; Xu, Y. Solid Sorbents for In-Situ CO_2 Removal during Sorption-Enhanced Steam Reforming Process: A Review. Renew. Sustain. Energy Rev. 2016, 53, 536–546. https://doi.org/10.1016/j.rser.2015.08.068.

(9) García-Díez, E.; Schaefer, S.; Sanchez-Sanchez, A.; Celzard, A.; Fierro, V.; Maroto-Valer, M. M.; García, S. Novel Porous Carbons Derived from Coal Tar Rejects: Assessment of the Role of Pore Texture in CO_2 Capture under Realistic Postcombustion Operating Temperatures. ACS Appl. Mater. Interfaces 2019, 11 (40), 36789–36799. https://doi.org/10.1021/acsami.9b13247.

(10) Samanta, A.; Zhao, A.; Shimizu, G. K. H.; Sarkar, P.; Gupta, R. Post-Combustion CO_2 Capture Using Solid Sorbents: A Review. Ind. Eng. Chem. Res. 2012, 51 (4), 1438–1463. https://doi.org/10.1021/ie200686q.

(11) Oyenekan, B. A.; Rochelle, G. T. Alternative Stripper Configurations for CO_2 Capture by Aqueous Amines. AIChE J. 2007, 53 (12), 3144–3154. https://doi.org/10.1002/aic.11316.

(12) Canevesi, R. L. S.; Andreassen, K. A.; Silva, E. A.; Borba, C. E.; Grande, C. A. Evaluation of Simplified Pressure Swing Adsorption Cycles for Bio-Methane Production. Adsorption 2019, 25 (0), 783–793. https://doi.org/10.1007/s10450-019-00049-x.

(13) Grande, C. A.; Blom, R. Utilization of Dual-PSA Technology for Natural Gas Upgrading and Integrated CO_2 Capture. 2012, 26, 2–14. https://doi.org/10.1016/j.egypro.2012.06.004.

(14) Canevesi, R. L. S.; Andreassen, K. A.; da Silva, E. A.; Borba, C. E.; Grande, C. A. Pressure Swing Adsorption for Biogas Upgrading with Carbon Molecular Sieve. Ind. Eng. Chem. Res. 2018, 57 (23), 8057–8067. https://doi.org/10.1021/acs.iecr.8b00996.

(15) Park, Y.; Moon, D.-K.; Kim, Y.-H.; Ahn, H.; Lee, C.-H. Adsorption Isotherms of CO_2, CO, N_2, CH_4, Ar and H_2 on Activated Carbon and Zeolite LiX up to 1.0 MPa. Adsorption 2014, 20 (4), 631–647. https://doi.org/10.1007/s10450-014-9608-x.

(16) Liang, Z.; Marshall, M.; Chaffee, A. L. CO_2 Adsorption-Based Separation by Metal Organic Framework (Cu-BTC) versus Zeolite (13X). Energy Fuels 2009, 23 (5), 2785–2789. https://doi.org/10.1021/ef800938e.

(17) Guo, B.; Chang, L.; Xie, K. Adsorption of Carbon Dioxide on Activated Carbon. J. Nat. Gas Chem. 2006, 15 (3), 223–229. https://doi.org/10.1016/S1003-9953(06)60030-3.

(18) Casco, M. E.; Martínez-Escandell, M.; Silvestre-Albero, J.; Rodríguez-Reinoso, F. Effect of the Porous Structure in Carbon Materials for CO_2 Capture at Atmospheric and High-Pressure. Carbon 2014, 67, 230–235. https://doi.org/10.1016/j.carbon.2013.09.086.
(19) Modak, A.; Jana, S. Advancement in Porous Adsorbents for Post-Combustion CO_2 Capture. Microporous Mesoporous Mater. 2019, 276, 107–132. https://doi.org/10.1016/j.micromeso.2018.09.018.
(20) Chen, J.; Loo, L. S.; Wang, K. High-Pressure CO_2 Adsorption on a Polymer-Derived Carbon Molecular Sieve. J. Chem. Eng. Data 2008, 53 (1), 2–4. https://doi.org/10.1021/je700178y.
(21) Hanif, A.; Dasgupta, S.; Nanoti, A. High Temperature CO_2 Adsorption by Mesoporous Silica Supported Magnesium Aluminum Mixed Oxide. Chem. Eng. J. 2015, 280, 703–710. https://doi.org/10.1016/j.cej.2015.06.018.
(22) Wickramaratne, N. P.; Jaroniec, M. Activated Carbon Spheres for CO_2 Adsorption. ACS Appl. Mater. Interfaces 2013, 5 (5), 1849–1855. https://doi.org/10.1021/am400112m.
(23) Ogungbenro, A. E.; Quang, D. V.; Al-Ali, K.; Abu-Zahra, M. R. M. Activated Carbon from Date Seeds for CO_2 Capture Applications. Energy Procedia 2017, 114, 2313–2321. https://doi.org/10.1016/j.egypro.2017.03.1370.
(24) Activated Carbons Prepared by the KOH Activation of a Hydrochar from Garlic Peel and Their CO_2 Adsorption Performance. New Carbon Mater. 2019, 34 (3), 247–257. https://doi.org/10.1016/S1872-5805(19)60014-4.
(25) Lee, S.-Y.; Park, S.-J. Determination of the Optimal Pore Size for Improved CO_2 Adsorption in Activated Carbon Fibers. J. Colloid Interface Sci. 2013, 389 (1), 230–235. https://doi.org/10.1016/j.jcis.2012.09.018.
(26) Wang, J.; Heerwig, A.; R. Lohe, M.; Oschatz, M.; Borchardt, L.; Kaskel, S. Fungi-Based Porous Carbons for CO_2 Adsorption and Separation. J. Mater. Chem. 2012, 22 (28), 13911–13913. https://doi.org/10.1039/C2JM32139D.
(27) Jang, E.; Choi, S. W.; Lee, K. B. Effect of Carbonization Temperature on the Physical Properties and CO_2 Adsorption Behavior of Petroleum Coke-Derived Porous Carbon. Fuel 2019, 248, 85–92. https://doi.org/10.1016/j.fuel.2019.03.051.
(28) Wang, L.; Rao, L.; Xia, B.; Wang, L.; Yue, L.; Liang, Y.; DaCosta, H.; Hu, X. Highly Efficient CO_2 Adsorption by Nitrogen-Doped Porous Carbons Synthesized with Low-Temperature Sodium Amide Activation. Carbon 2018, 130, 31–40. https://doi.org/10.1016/j.carbon.2018.01.003.
(29) Han, J.; Zhang, L.; Zhao, B.; Qin, L.; Wang, Y.; Xing, F. The N-Doped Activated Carbon Derived from Sugarcane Bagasse for CO_2 Adsorption. Ind. Crops Prod. 2019, 128, 290–297. https://doi.org/10.1016/j.indcrop.2018.11.028.
(30) Ma, C.; Lu, T.; Shao, J.; Huang, J.; Hu, X.; Wang, L. Biomass Derived Nitrogen and Sulfur Co-Doped Porous Carbons for Efficient CO_2 Adsorption. Sep. Purif. Technol. 2022, 281, 119899. https://doi.org/10.1016/j.seppur.2021.119899.
(31) Zhao, Z.; Ma, C.; Chen, F.; Xu, G.; Pang, R.; Qian, X.; Shao, J.; Hu, X. Water Caltrop Shell-Derived Nitrogen-Doped Porous Carbons with High CO_2 Adsorption Capacity. Biomass Bioenergy 2021, 145, 105969. https://doi.org/10.1016/j.biombioe.2021.105969.
(32) Liu, S.; Rao, L.; Yang, P.; Wang, X.; Wang, L.; Ma, R.; Yue, L.; Hu, X. Superior CO_2 Uptake on Nitrogen Doped Carbonaceous Adsorbents from Commercial Phenolic Resin. J. Environ. Sci. China 2020, 93, 109–116. https://doi.org/10.1016/j.jes.2020.04.006.
(33) Plaza, M. G.; Pevida, C.; Arenillas, A.; Rubiera, F.; Pis, J. J. CO_2 Capture by Adsorption with Nitrogen Enriched Carbons. Fuel 2007, 86 (14), 2204–2212. https://doi.org/10.1016/j.fuel.2007.06.001.
(34) Liu, C.; Xing, W.; Zhou, J.; Zhuo, S. N-Containing Activated Carbons for CO_2 Capture. Int. J. Smart Nano Mater. 2013, 4 (1), 55–61. https://doi.org/10.1080/19475411.2012.668861.
(35) Sevilla, M.; Valle-Vigón, P.; Fuertes, A. B. N-Doped Polypyrrole-Based Porous Carbons for CO_2 Capture. Adv. Funct. Mater. 2011, 21 (14), 2781–2787. https://doi.org/10.1002/adfm.201100291.

(36) Braghiroli, F. L.; Fierro, V.; Izquierdo, M. T.; Parmentier, J.; Pizzi, A.; Delmotte, L.; Fioux, P.; Celzard, A. High Surface – Highly N-Doped Carbons from Hydrothermally Treated Tannin. Ind. Crops Prod. 2015, 66, 282–290. https://doi.org/10.1016/j.indcrop.2014.11.022.
(37) Braghiroli, F. L.; Fierro, V.; Szczurek, A.; Stein, N.; Parmentier, J.; Celzard, A. Electrochemical Performances of Hydrothermal Tannin-Based Carbons Doped with Nitrogen. Ind. Crops Prod. 2015, 70, 332–340. https://doi.org/10.1016/j.indcrop.2015.03.046.
(38) Braghiroli, F. L.; Fierro, V.; Szczurek, A.; Stein, N.; Parmentier, J.; Celzard, A. Hydrothermally Treated Aminated Tannin as Precursor of N-Doped Carbon Gels for Supercapacitors. Carbon 2015, 90, 63–74. https://doi.org/10.1016/j.carbon.2015.03.038.
(39) Horikawa, T.; Sakao, N.; Sekida, T.; Hayashi, J.; Do, D. D.; Katoh, M. Preparation of Nitrogen-Doped Porous Carbon by Ammonia Gas Treatment and the Effects of N-Doping on Water Adsorption. Carbon 2012, 50 (5), 1833–1842. https://doi.org/10.1016/j.carbon.2011.12.033.
(40) Stöhr, B.; Boehm, H. P.; Schlögl, R. Enhancement of the Catalytic Activity of Activated Carbons in Oxidation Reactions by Thermal Treatment with Ammonia or Hydrogen Cyanide and Observation of a Superoxide Species as a Possible Intermediate. Carbon 1991, 29 (6), 707–720. https://doi.org/10.1016/0008-6223(91)90006-5.
(41) Rao, L.; Ma, R.; Liu, S.; Wang, L.; Wu, Z.; Yang, J.; Hu, X. Nitrogen Enriched Porous Carbons from D-Glucose with Excellent CO_2 Capture Performance. Chem. Eng. J. 2019, 362, 794–801. https://doi.org/10.1016/j.cej.2019.01.093.
(42) Chen, J.; Yang, J.; Hu, G.; Hu, X.; Li, Z.; Shen, S.; Radosz, M.; Fan, M. Enhanced CO_2 Capture Capacity of Nitrogen-Doped Biomass-Derived Porous Carbons. ACS Sustain. Chem. Eng. 2016, 4 (3), 1439–1445. https://doi.org/10.1021/acssuschemeng.5b01425.
(43) Balahmar, N.; Mitchell, A. C.; Mokaya, R. Generalized Mechanochemical Synthesis of Biomass-Derived Sustainable Carbons for High Performance CO_2 Storage. Adv. Energy Mater. 2015, 5 (22), 1500867. https://doi.org/10.1002/aenm.201500867.
(44) Yue, L.; Xia, Q.; Wang, L.; Wang, L.; DaCosta, H.; Yang, J.; Hu, X. CO_2 Adsorption at Nitrogen-Doped Carbons Prepared by K2CO3 Activation of Urea-Modified Coconut Shell. J. Colloid Interface Sci. 2018, 511, 259–267. https://doi.org/10.1016/j.jcis.2017.09.040.
(45) Liu, S.; Yang, P.; Wang, L.; Li, Y.; Wu, Z.; Ma, R.; Wu, J.; Hu, X. Nitrogen-Doped Porous Carbons from Lotus Leaf for CO_2 Capture and Supercapacitor Electrodes. Energy Fuels 2019, 33 (7), 6568–6576. https://doi.org/10.1021/acs.energyfuels.9b00886.
(46) Sánchez-Sánchez, Á.; Suárez-García, F.; Martínez-Alonso, A.; Tascón, J. M. D. Influence of Porous Texture and Surface Chemistry on the CO_2 Adsorption Capacity of Porous Carbons: Acidic and Basic Site Interactions. ACS Appl. Mater. Interfaces 2014, 6 (23), 21237–21247. https://doi.org/10.1021/am506176e.
(47) Zhao, W.; Fierro, V.; Fernández-Huerta, N.; Izquierdo, M. T.; Celzard, A. Hydrogen Uptake of High Surface Area-Activated Carbons Doped with Nitrogen. Int. J. Hydrog. Energy 2013, 38 (25), 10453–10460. https://doi.org/10.1016/j.ijhydene.2013.06.048.
(48) Jagiello, J.; Kenvin, J.; Ania, C. O.; Parra, J. B.; Celzard, A.; Fierro, V. Exploiting the Adsorption of Simple Gases O_2 and H_2 with Minimal Quadrupole Moments for the Dual Gas Characterization of Nanoporous Carbons Using 2D-NLDFT Models. Carbon 2020, 160, 164–175. https://doi.org/10.1016/j.carbon.2020.01.013.
(49) Ramirez-Vidal, P.; Canevesi, R. L. S.; Sdanghi, G.; Schaefer, S.; Maranzana, G.; Celzard, A.; Fierro, V. A Step Forward in Understanding the Hydrogen Adsorption and Compression on Activated Carbons. ACS Appl. Mater. Interfaces 2021, 13 (10), 12562–12574. https://doi.org/10.1021/acsami.0c22192.
(50) Jansen, R. J. J.; van Bekkum, H. XPS of Nitrogen-Containing Functional Groups on Activated Carbon. Carbon 1995, 33 (8), 1021–1027. https://doi.org/10.1016/0008-6223(95)00030-H.
(51) Schaefer, S.; Jeder, A.; Sdanghi, G.; Gadonneix, P.; Abdedayem, A.; Izquierdo, M. T.; Maranzana, G.; Ouederni, A.; Celzard, A.; Fierro, V. Oxygen-Promoted Hydrogen Adsorption on Activated and Hybrid Carbon Materials. Int. J. Hydrog. Energy 2020. https://doi.org/10.1016/j.ijhydene.2020.08.114.

(52) Celzard, A.; Pasc, A.; Schaefer, S.; Mandel, K.; Ballweg, T.; Li, S.; Medjahdi, G.; Nicolas, V.; Fierro, V. Floating Hollow Carbon Spheres for Improved Solar Evaporation. Carbon 2019, 146, 232–247. https://doi.org/10.1016/j.carbon.2019.01.101.
(53) Sips, R. On the Structure of a Catalyst Surface. J. Chem. Phys. 1948, 16 (5), 490–495. https://doi.org/10.1063/1.1746922.
(54) Thommes, M.; Kaneko, K.; Neimark, A. V.; Olivier, J. P.; Rodriguez-Reinoso, F.; Rouquerol, J.; Sing, K. S. W. Physisorption of Gases, with Special Reference to the Evaluation of Surface Area and Pore Size Distribution (IUPAC Technical Report). Pure Appl. Chem. 2015, 87 (9–10). https://doi.org/10.1515/pac-2014-1117.
(55) Gokce, Y.; Aktas, Z. Nitric Acid Modification of Activated Carbon Produced from Waste Tea and Adsorption of Methylene Blue and Phenol. Appl. Surf. Sci. 2014, 313, 352–359. https://doi.org/10.1016/j.apsusc.2014.05.214.
(56) Jaramillo, J.; Álvarez, P. M.; Gómez-Serrano, V. Oxidation of Activated Carbon by Dry and Wet Methods. Fuel Process. Technol. 2010, 91 (11), 1768–1775. https://doi.org/10.1016/j.fuproc.2010.07.018.
(57) Hulicova-Jurcakova, D.; Seredych, M.; Lu, G. Q.; Bandosz, T. J. Combined Effect of Nitrogen- and Oxygen-Containing Functional Groups of Microporous Activated Carbon on Its Electrochemical Performance in Supercapacitors. Adv. Funct. Mater. 2009, 19 (3), 438–447. https://doi.org/10.1002/adfm.200801236.
(58) Mostazo-López, M. J.; Ruiz-Rosas, R.; Morallón, E.; Cazorla-Amorós, D. Generation of Nitrogen Functionalities on Activated Carbons by Amidation Reactions and Hofmann Rearrangement: Chemical and Electrochemical Characterization. Carbon 2015, 91, 252–265. https://doi.org/10.1016/j.carbon.2015.04.089.
(59) Maziarka, P.; Wurzer, C.; Arauzo, P. J.; Dieguez-Alonso, A.; Mašek, O.; Ronsse, F. Do You BET on Routine? The Reliability of N_2 Physisorption for the Quantitative Assessment of Biochar's Surface Area. Chem. Eng. J. 2021, 418, 129234. https://doi.org/10.1016/j.cej.2021.129234.
(60) Acosta, R.; Nabarlatz, D.; Sánchez-Sánchez, A.; Jagiello, J.; Gadonneix, P.; Celzard, A.; Fierro, V. Adsorption of Bisphenol A on KOH-Activated Tyre Pyrolysis Char. J. Environ. Chem. Eng. 2018, 6 (1), 823–833. https://doi.org/10.1016/j.jece.2018.01.002.
(61) Bashkova, S.; Bandosz, T. J. The Effects of Urea Modification and Heat Treatment on the Process of NO_2 Removal by Wood-Based Activated Carbon. J. Colloid Interface Sci. 2009, 333 (1), 97–103. https://doi.org/10.1016/j.jcis.2009.01.052.
(62) Arenillas, A.; Rubiera, F.; Parra, J. B.; Ania, C. O.; Pis, J. J. Surface Modification of Low Cost Carbons for Their Application in the Environmental Protection. Appl. Surf. Sci. 2005, 252 (3), 619–624. https://doi.org/10.1016/j.apsusc.2005.02.076.
(63) Braghiroli, F. L.; Fierro, V.; Izquierdo, M. T.; Parmentier, J.; Pizzi, A.; Celzard, A. Nitrogen-Doped Carbon Materials Produced from Hydrothermally Treated Tannin. Carbon 2012, 50 (15), 5411–5420. https://doi.org/10.1016/j.carbon.2012.07.027.
(64) Mostazo-López, M. J.; Salinas-Torres, D.; Ruiz-Rosas, R.; Morallón, E.; Cazorla-Amorós, D. Nitrogen-Doped Superporous Activated Carbons as Electrocatalysts for the Oxygen Reduction Reaction. Materials 2019, 12 (8). https://doi.org/10.3390/ma12081346.
(65) Grande, C. A.; Gigola, C.; Rodrigues, A. E. Propane–Propylene Binary Adsorption on Zeolite 4A. Adsorption 2003, 9 (4), 321–329. https://doi.org/10.1023/A:1026223914143.
(66) Rocha, L. A. M.; Andreassen, K. A.; Grande, C. A. Separation of CO_2/CH_4 Using Carbon Molecular Sieve (CMS) at Low and High Pressure. Chem. Eng. Sci. 2017, 164, 148–157. https://doi.org/10.1016/j.ces.2017.01.071.
(67) Grande, C. A.; Blom, R.; Middelkoop, V.; Matras, D.; Vamvakeros, A.; Jacques, S. D. M.; Beale, A. M.; Di Michiel, M.; Anne Andreassen, K.; Bouzga, A. M. Multiscale Investigation of Adsorption Properties of Novel 3D Printed UTSA-16 Structures. Chem. Eng. J. 2020, 126166. https://doi.org/10.1016/j.cej.2020.126166.

(68) He, J.; To, J.; Mei, J.; Bao, Z.; Wilcox, J. Facile Synthesis of Nitrogen-Doped Porous Carbon for Selective CO_2 Capture. Energy Procedia 2014, 63, 2144–2151. https://doi.org/10.1016/j.egypro.2014.11.233.
(69) Alabadi, A.; Abbood, H. A.; Li, Q.; Jing, N.; Tan, B. Imine-Linked Polymer Based Nitrogen-Doped Porous Activated Carbon for Efficient and Selective CO_2 Capture. Sci. Rep. 2016, 6 (1), 1–9. https://doi.org/10.1038/srep38614.
(70) Hu, X.; Radosz, M.; Cychosz, K. A.; Thommes, M. CO_2 -Filling Capacity and Selectivity of Carbon Nanopores: Synthesis, Texture, and Pore-Size Distribution from Quenched-Solid Density Functional Theory (QSDFT). Environ. Sci. Technol. 2011, 45 (16), 7068–7074. https://doi.org/10.1021/es200782s.
(71) Bae, J.-S.; Bhatia, S. K. High-Pressure Adsorption of Methane and Carbon Dioxide on Coal. Energy Fuels 2006, 20 (6), 2599–2607. https://doi.org/10.1021/ef060318y.
(72) Song, Y.; Xing, W.; Zhang, Y.; Jian, W.; Liu, Z.; Liu, S. Adsorption Isotherms and Kinetics of Carbon Dioxide on Chinese Dry Coal over a Wide Pressure Range. Adsorption 2015, 21 (1), 53–65. https://doi.org/10.1007/s10450-015-9649-9.

For Table of Contents Only